

Radio-Frequency Side-Channel Analysis of a Trapped-Ion Quantum Computer

Giorgio Grigolo,^{1,2,*} Dorian Schiffer,^{1,2,†} Lukas Gerster,^{3,‡} Martin Ringbauer,^{3,§} and Paul Erker^{1,2,¶}

¹Atominstut, Technische Universität Wien, Stadionallee 2, 1020 Vienna, Austria

²Institute for Quantum Optics and Quantum Information (IQOQI),

Austrian Academy of Sciences, Boltzmannngasse 3, 1090 Vienna, Austria

³Institut für Experimentalphysik, Universität Innsbruck, Technikerstraße 25, 6020 Innsbruck, Austria

(Dated: March 9, 2026)

Analogously to classical computers, quantum processors exhibit side channels that may give attackers access to potentially proprietary algorithms. We identify and exploit a previously unexplored side channel in trapped-ion quantum processors that arises from the radio-frequency (RF) signals used to modulate lasers for ion cooling, gate execution, and readout. In these quantum processors, acousto-optical modulators (AOMs) imprint phase and frequency modulations onto laser fields interacting with the ions to implement individual and collective unitaries. The AOMs are driven by strong RF signals, a fraction of which leaks out of the device. We discuss general strategies to exploit this side channel and demonstrate how to detect RF leakage from a state-of-the-art qudit-based quantum processor using off-the-shelf components. From this data, we extract pulse characteristics of single-ion and entangling gates, thereby implementing a proof-of-principle exploitation of the novel attack vector. Finally, we outline ways to mitigate the information leakage through the presented side channel.

I. INTRODUCTION

The race to build the first universal quantum computer is well underway, with a range of hardware platforms developing rapidly, including superconducting qubits, neutral atoms, trapped ions, or photonic systems, to name a few [1–12]. In parallel, the community is exploring *qudit*-based processors, which promise more efficient information processing in applications such as quantum simulation [13–18]. Alongside these advances, researchers are already examining the security of such systems: although quantum information itself cannot be perfectly copied [19], quantum computers share several vulnerabilities with their classical counterparts. In classical systems, such as hardware cryptographic implementations, an important type of attack exploits side channels, i.e. unintended information leakage. Side-channel attacks are typically classified by their source of leakage, such as timing information, power consumption, electromagnetic (EM) emanations, or acoustic emissions [20–23].

Quantum computers also present side channels that, given sufficient physical access, could be exploited to extract sensitive information about the computation being performed at a given time. Security researchers have so far only identified a limited number of side channels in quantum computers [24–27]. For instance, the power trace of the control hardware was shown to be sufficient to perform circuit reconstruction [28, 29]. Side-channel attacks that involve power analysis typically require an attacker to physically attach a power meter to the target device. In contrast, we identify and exploit an attack vector for trapped-ion systems based on EM leakages that neither requires any modification of the existing architecture of the quantum processing unit (QPU), nor access to its power lines. Hence, our method can be classified as

a *passive, non-invasive, and profiled* side-channel attack [30–32]. The data acquisition setup used for the experimental proof-of-principle implementation of the attack, illustrated in Fig. 1, is composed of commercially available, off-the-shelf components and operates completely independently of the target system. Because this attack requires no modification to the quantum processor, it represents a more practical and immediate security threat than previously reported side-channel vulnerabilities.

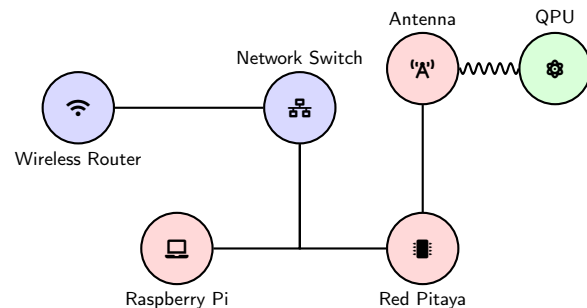


Figure 1. High level topology of the hardware for remote data acquisition, consisting of network devices (blue), the attacker hardware (red) and the QPU (green).

II. TRAPPED-ION CONTROL SIDE CHANNEL

The operating principle of the target trapped-ion quantum computer [33, 34] is to process quantum information within internal electronic energy levels of a string of $^{40}\text{Ca}^+$ ions confined in a linear Paul trap. Gate operations are performed by modulating narrow-band resonant laser light using RF drive signals, which presents a side channel.

A. Physical Background

The QPU achieves high dimensionality by using permanent magnets, generating a magnetic field of about 7.5G that lifts the degeneracy of the electronic energy levels, allowing individual ions to host qudits with up to 8 states each. By coupling the electronic states of individual ions in a linear chain to their collective motion within the trap, one may create entanglement between different ions. Quantum gate operations then correspond to unitary rotations of the spin associated to a particular transition, i.e., controlled Rabi oscillations between the relevant energy levels. After all circuit unitaries are executed, the qudit state is read out by iterative electron shelving between the fluorescing ground state and the dark excited states [34].

Laser cooling, gate execution, and readout are performed using several laser systems guided into the vacuum chamber holding the ion trap. Each laser passes through one or more *acousto-optical modulators* (AOMs) along its optical path. These devices consist of a piezoelectric transducer attached to a crystal medium. When driven by a strong RF signal, the piezo creates standing acoustic waves in the crystal. Light passing through the AOM is then scattered off a diffraction grating realised by periodic density fluctuations, thereby imprinting a transverse momentum kick, a frequency shift, and a phase onto the light beam. Hence, AOMs are used to generate laser pulses, route lasers, and tune the laser frequency, amplitude, and phase for different electronic transitions.

In particular, AOMs play a central role in the implementation of gates. By steering a laser of fixed amplitude to an individual ion and shifting its frequency to match the target transition from level $|i\rangle$ to $|j\rangle$, the electronic state undergoes Rabi oscillations with the angular frequency Ω . By choosing the amplitude, duration, and phase of the pulse aimed at the ion correspondingly, one can implement any rotation of the spin state. In the Bloch sphere picture, we denote the polar angle by θ and the azimuthal angle by ϕ . Then, the pulse duration τ sets θ via $\theta \propto \Omega\tau$, while the phase of the pulse ϕ determines around which axis in the equatorial plane one rotates. Altogether, the pulses implement the unitary

$$\mathbf{R}^{i,j}(\theta, \phi) = \exp\left[-\frac{i\theta}{2}\sigma_\phi^{i,j}\right] \quad (1)$$

where i and j label the two sub-levels of the addressed ion. Here, $\sigma_\phi^{i,j} = \cos\phi\sigma_x^{i,j} \pm \sin\phi\sigma_y^{i,j}$, with Pauli matrices $\sigma_x^{i,j}$ and $\sigma_y^{i,j}$, generates coherent rotations between levels i and j with the azimuthal angle ϕ determining around which equatorial axis the rotations are performed [34].

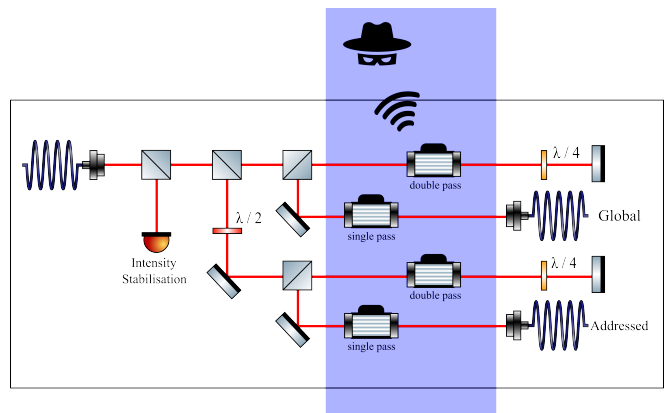


Figure 2. Quadrupole laser switching setup of the target quantum processor [35], highlighting the region from which the informationally rich RF signal emissions leak.

The entangling Mølmer-Sørensen gate [36] employs the aforementioned generator, but this time the laser pulses are routed to pairs of ions, enacting the unitary

$$\text{MS}^{i,j}(\theta, \phi) = \exp\left[-\frac{i\theta}{4}\left(\sigma_\phi^{i,j} \otimes \mathbb{1} + \mathbb{1} \otimes \sigma_\phi^{i,j}\right)^2\right], \quad (2)$$

where $\mathbb{1}$ denotes the identity transformation on the other ion. Note that typically the laser powers required for the entangling gate are significantly higher than for the individual-ion gates, since the former relies on the excitation of the shared motional mode within the trap.

The specifications of any single-ion gate implemented in such a way can be inferred from the RF signal driving the relevant AOMs. Its *frequency* labels the addressed transition, its *duration* – in cases where Ω is known – determines θ , and its *phase* corresponds to ϕ . In addition, the addressing of different ions within the trap relies on *acousto-optical deflectors* (AODs), which work similarly to AOMs. Hence, the AOD drive signals reveal which ions gates are applied to and since they are correlated with the gate sequence being executed, they constitute a serious information leak in themselves that we specifically target. Furthermore, the laser intensity (or Rabi frequency) on the ion is determined by the *intensity* of the RF drive pulses. This information is used to mitigate intensity-caused drifts in the Rabi frequency and in combination with the monitoring the addressing AODs, helps to distinguish the entangling MS gate, which requires higher laser powers.

The strong RF signals driving the acousto-optical components generate electromagnetic emissions leaking through any insufficiently shielded parts of the setup. These leakages carry information about the quantum circuit being executed and thereby constitute a side channel.

B. Practical Considerations

Most quantum processors employ a finite, typically small, set of native gates that can be executed directly and that together form a universal gate set [37]. We assume that all quantum circuits are compiled exclusively into the following native and universal gate set. In our analysis, we consider

$$\begin{aligned} R_x^{i,j}(\theta) &= R^{i,j}(\theta, 0) \text{ and} \\ R_y^{i,j}(\theta) &= R^{i,j}(\theta, \pi/2) \end{aligned} \quad (3)$$

as the single-qudit gates available to an attacker, with $\theta \in (0, 2\pi)$. Corresponding to rotations around the x - and y -axes, they enable the construction of arbitrary single-qudit unitaries via Euler decompositions [37, 38].

Entangling operations are supplied by the Mølmer–Sørensen (MS) gate with fixed parameters $\theta = \pi/2$ and $\phi = 0$, acting on the transition from level i to j in two different ions. We denote this operation by $MS^{i,j} = MS^{i,j}(\pi/2, 0)$ to achieve maximal entanglement. The resulting native, universal gate set available to an attacker is, therefore,

$$\Gamma = \{R_x^{i,j}(\theta), R_y^{i,j}(\theta), MS^{i,j}\} \quad (5)$$

for all transitions $|i\rangle \leftrightarrow |j\rangle$ with $i < j$ and qudit pairs within the trapped-ion chain.

The above assumptions are asserted to allow and simplify an enumeration attack, by reducing the number of parameters an attacker must consider in their eventual attempt to reconstruct the circuit being executed. In particular, we restrict ϕ to only two values, namely $\phi = 0$ and $\phi = \pi/2$, and choose θ to lie within $(0, 2\pi]$. We note that this setting is more reminiscent of future fault-tolerant devices that must use a discrete gate set. Current noisy intermediate-scale quantum computing (NISQ) devices, on the other hand, tend to work with continuous phase parameters, which can in principle be accommodated by the proposed method.

III. METHODS OF ANALYSIS

We describe two complementary paradigms in our approach to distinguish different gates based on leaked RF emissions, followed by a detailed account of our data acquisition and signal processing procedures.

A. Frameworks for Circuit Reconstruction

As shown in the previous section, the pulses in the leaked RF emissions, in principle, contain the complete

information that specifies a circuit. This motivates a physics-driven approach in which the attack does not rely on a training step or prior interaction with the QPU. Instead, it exploits detailed knowledge of the underlying trapped-ion system, including ion dynamics, trap parameters, and control field interactions, to infer the pulse durations, amplitudes, and phases that uniquely determine the implemented unitary operation. By modeling the relationship between the applied control pulses and the resulting state evolution, this approach aims to identify gates directly from leaked RF emissions during execution.

However, this methodology implicitly assumes access to high-end measurement hardware, including high-bandwidth receivers, high sampling rates, and low noise floors, as well as precise synchronization and accurate spectral estimation techniques. Moreover, any QPU requires periodic calibration, which must also be taken into account. In particular, resolving the relevant control features requires careful time-frequency analysis to mitigate uncertainty arising from the Fourier limit. Finally, one must also consider that, in general not all the relevant system parameters and control models are publicly available or theoretically derivable, and even if they are, effectively leveraging this information in practice might entail non-trivial analytical and computational effort.

An alternative attempt to differentiate gates is to employ a data-driven approach, that generically requires the attacker to interact with the QPU to build a training library, for instance by submitting circuits [39]. An advantage of this method is that it abstracts away most of the physics of the underlying system, including slight variations in control signals caused by calibration drift, or device-specific idiosyncrasies. Here, we assume the attacker is able to construct and execute a quantum circuit that contains all the native gates that are used for universality. The attacker then measures the RF emissions caused by the execution of this circuit and associates a specific gate to one or more pulses extracted from the RF emissions. These associations could then be used to build a classifier that ingests an unknown sequence of pulses and predicts the most likely sequence of gates that produced them, making this approach fully learning-based [40].

It stands to reason that the RF emissions of interest cannot be meaningfully analysed in isolation from the physical processes that generate them, as to some extent, they must ultimately reflect the underlying control fields and ion dynamics. A hybrid approach is likely most effective: physical insight can guide and constrain pre-processing and feature extraction, while data-driven methods can improve robustness to noise and variability.

B. Data Acquisition

To monitor the RF emissions of interest while suppressing noise in the relevant frequency range, we deploy two low-gain sniffing antennae constructed from BNC cables that are stripped at one end, purposefully designed to appear like dangling wires. One antenna is placed in proximity to the magnetic shield, which contains the addressing optics. The second antenna is located roughly 30 cm above the AOMs responsible for pulse generation during gate operations. Signals from both antennae are routed through band pass filters B_{RF1} and B_{RF2} (see Fig. 3) with pass-bands 27.5–200 MHz and 90–400 MHz respectively, to further reduce out-of-band noise and interference, into the input channels of a RED PITAYA SDRLAB 122-16 data acquisition board with a sampling rate of 122.88 MS/s.

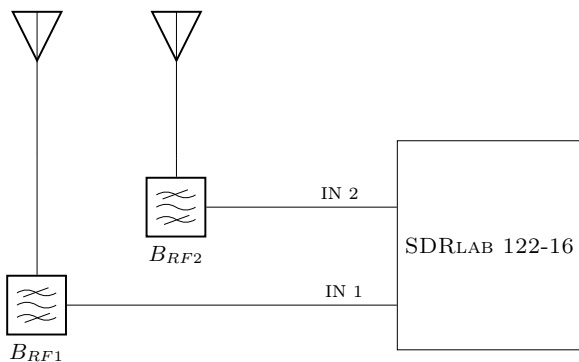


Figure 3. Schematic diagram of the SDRLAB 122-16-based receiver system with two antennae and bandpass filters.

Since the AOM drive frequencies roughly lie between 80 MHz and 250 MHz [35], the measured RF emissions are subject to aliasing and thus folded into the Nyquist band, namely to frequencies below $f_s/2$, where f_s is the sampling rate of the acquisition system. One could in principle work out possible signal frequencies f_{sig} from the measured aliased frequencies by manipulating the relation $f_{\text{alias}} = |f_{\text{sig}} - kf_s|$ into

$$f_{\text{sig}} = |kf_s \pm f_{\text{alias}}|, \quad (6)$$

while varying the integer k until f_{sig} falls within the expected range of AOM drive frequencies, or corresponds to a frequency that – imprinted on a laser – will address a known ion transition.

As illustrated in Fig. 1, due to the acquisition setup connection to the Internet, data acquisition can be triggered from an arbitrary location, without the need for precise synchronization with the QPU. Most quantum computer job submission platforms provide the option to run a circuit multiple times (*shots*) in succession, with some delay between shots. With a sufficiently large num-

ber of shots, the attacker has more time available to successfully initiate data acquisition, and can thus capture the RF emissions without requiring tight synchronization.

C. Signal Processing

Here we describe our signal processing pipeline to extract pulse events from the raw RF emissions. A sample of the raw RF signal recorded from one of the antennae during the execution of a quantum circuit is shown in Fig. 4.

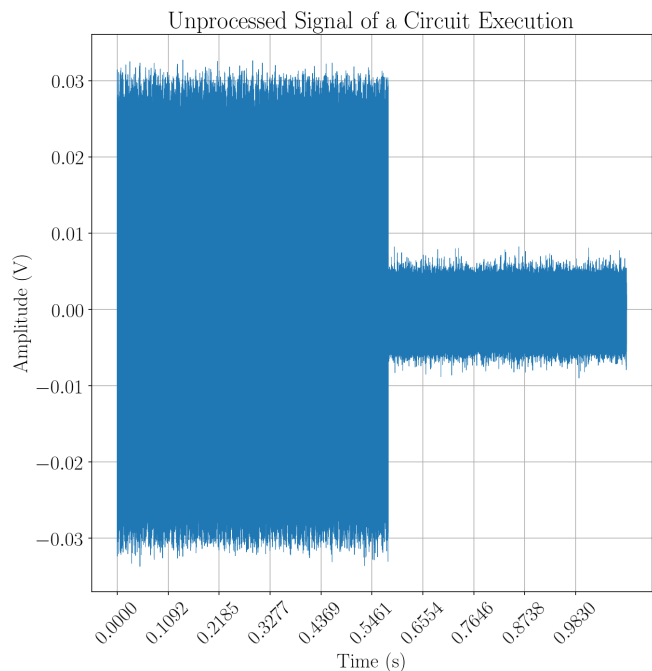


Figure 4. A high energy segment is clearly visible in the RF emissions recorded, indicating that some control activity is taking place.

After acquiring approximately one second of filtered RF emission $x(t)$, a region of interest is selected, such that it corresponds to control activity during circuit execution. This region is trivially observable as a high-energy segment in the recorded signal such as in Fig. 4. Data outside this interval is discarded, and, if desired, a shorter fixed-length segment within the region is selected to reduce the computational cost of subsequent processing. Individual pulse events are then identified within the selected high-power region.

Pulse detection is carried out in the time-frequency representation obtained from a short-time Fourier transform (STFT) with a Hann window of length $N_{\text{seg}} = 2048$ bins and overlap $N_{\text{ov}} = 1024$ bins, fixed empirically to balance temporal and spectral resolution. Let $X(f, t)$

denote the resulting complex-valued STFT, where f and t index frequency bins and time frames, respectively. The power spectrogram is then given by $S(f, t) = |X(f, t)|^2$. To identify significant transient events, we compute a global detection threshold based on the spectrogram power statistics. We averaged power over time as

$$\mu(f) \equiv \frac{1}{N_t} \sum_t S(f, t), \quad (7)$$

where N_t is the number of time frames in the one-sided STFT. Let

$$\bar{\mu} = \frac{1}{N_f} \sum_f \mu(f) \quad \text{and} \quad \sigma_\mu = \sqrt{\frac{1}{N_f} \sum_f (\mu(f) - \bar{\mu})^2},$$

where N_f is the number of frequency bins of the STFT with the given window parameters. The global detection threshold is then defined as

$$\mathcal{T} = \bar{\mu} + \alpha \sigma_\mu, \quad (8)$$

with α a fixed constant controlling the sensitivity to excursions above the background. Time-frequency points satisfying $S(f, t) > \mathcal{T}$ are retained, yielding a binary detection mask used for subsequent pulse identification.

Connected components in the binary time-frequency mask are identified using two-dimensional connected-component labeling with fixed connectivity (8-connectivity) [41]. Each connected component is interpreted as an individual pulse event. For each component, the pulse start and end times t_s and t_e , are defined by the minimum and maximum time indices, respectively, and the pulse duration τ is given by $\tau = t_e - t_s$. A representative centre frequency f_c is computed as the power-weighted mean frequency over all bins belonging to the component, effectively capturing the dominant frequency content of the pulse. The algorithm outputs a set of detected pulses parametrised by $\{t_s, t_e, \tau, f_c\}$. Figures 7 and 8 in Appendix A illustrate the results of the pulse detection algorithm applied to one shot.

Currently, pulse intensity information is not included. As discussed in Section II A, intensity may be informative, as it correlates with variations in the Rabi frequency. However, actually harnessing this information would require detailed knowledge of signal losses and antenna gain. Given that it is in the interest of the QPU users to minimize power fluctuations, we operate under the assumption that laser powers are constant. Due to a current limitation of our setup, phase information is not yet available to us. We recognize the importance of incorporating intensity and phase features for full circuit reconstruction, for instance, in the context of optimal pulse shaping [42, 43], and we aim to include it in future work.

D. Shot Extraction and Analysis

Once an array of pulses has been extracted, we proceed by sectioning the region of interest into individual shots. We first sort the array of pulses by their start time and, if necessary, by their centre frequency to break ties. We then observe the gaps in time between consecutive pulses in this sorted order, by computing $t_e^{(i+1)} - t_s^{(i)}$, as shown in Fig. 5.

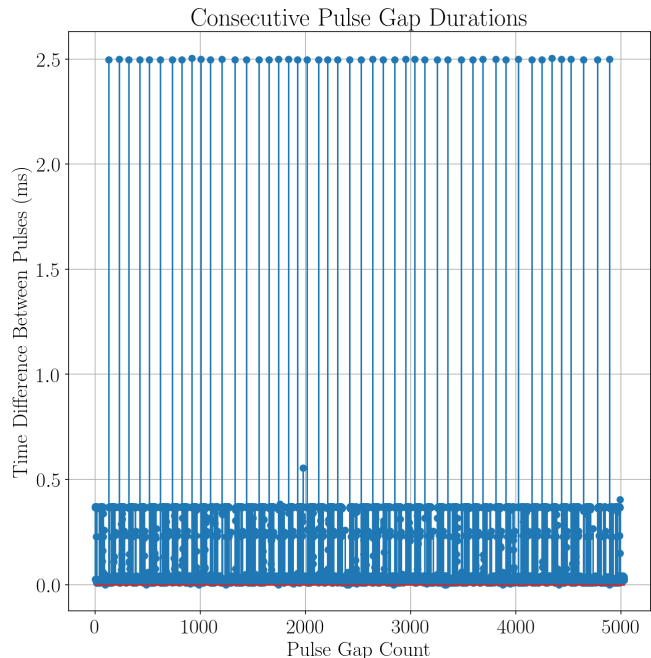


Figure 5. The time differences between consecutive pulses exhibit clear patterns, which reveal the target quantum processor’s delay between shots, at around 2.5 ms.

As illustrated in Fig. 5 the values that arise for the gap durations, remain very consistent. We then take the pulses in between these markers to be our shots. This allows us to analyse individual circuit shots and their constituent pulses, while reasoning about what control operations they correspond to. We refer to the regions A , B , and C in Figs. 7 and 8 in Appendix A, to denote different stages of circuit execution in the target QPU.

In region A we observe a pre-processing stage which may include a combination of Doppler cooling, side-band cooling, and polarisation gradient cooling, as well as optical pumping for state initialisation and preparation [34]. An attacker may determine this section by submitting an empty circuit for execution, and observing that pulses are still emitted in a specific pattern during this phase. Region B corresponds to the core section of the circuit execution pipeline, i.e. where the gate operations are performed. An attacker may analyse

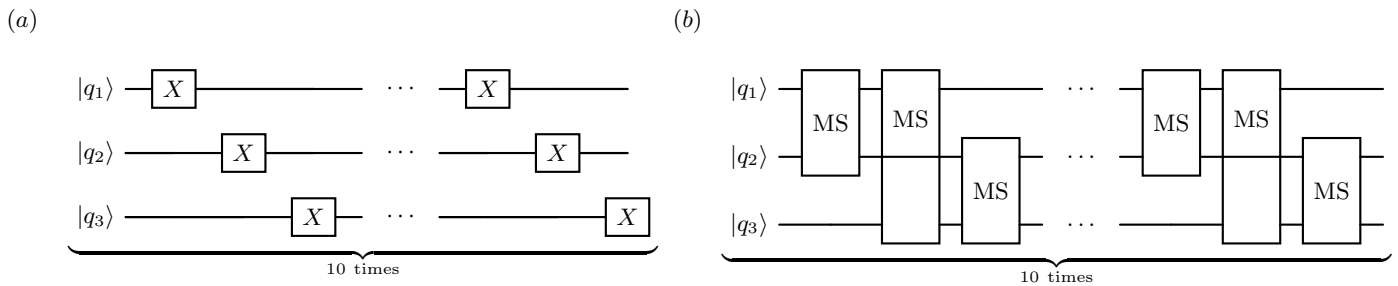


Figure 6. Circuit diagrams of sequential applications of (a) $X = R_x^{0,1}(\pi)$ gates on qutrits q_1, q_2, q_3 , and (b) of $MS = MS^{0,1}$ on every combination of qutrit pairs.

this section by submitting circuits that contain only single-qutrit or only two-qutrit gates, to then collect the corresponding pulse features for further analysis. Region C corresponds to the final readout stage, where the target QPU performs a sequence of cooling and detection operations for every $|i\rangle \leftrightarrow |j\rangle$ transition [34]. An attacker may identify this section by noting that the readout step – similar to region A – tends to contain very consistent pulse parameters and longer pulse durations that are independent of the circuit executed.

IV. EXPERIMENTAL FINDINGS

Given the aforementioned capabilities, namely physical access to the quantum processor and the ability to execute arbitrary circuits, an adversary is in a favourable position to systematically construct circuits that maximize the information yield, enabling more effective discrimination between quantum gates. In this section, we choose two representative circuits and describe the information that one may obtain, as well as the implications for circuit reconstruction. One such circuit is shown in Fig. 6(a), where we apply $X = R_x^{0,1}(\pi)$ gates sequentially on three different ions, and repeat this sequence ten times. This circuit is designed to elicit clear and consistent pulse fingerprints correlated to the X gates across different ions. Similarly, this could be repeated for $Y = R_y^{0,1}(\pi)$ gates, and possibly for different values of θ to construct a more comprehensive dataset of pulse features to be used for gate classification.

However, we note that the targeted transitions could not yet be inferred, as the double-pass AOMs handling gate preparations were operated at significantly lower power than anticipated, and any resulting leakage was not detectable with our current antennae. Unfortunately, this entails that we must leave qutrit gate resolution to future iterations of the experiment. Instead, we detect and analyse the addressing pulses, characterised by the step-like pattern between 5 MHz and 10 MHz in Region B of Figs. 7 and 8.

The measured ion addressing frequencies in Table. I, and the sequential nature of the ions we choose to apply the gates on, as in the circuits in Figs. 6(a) and 6(b) allow to uniquely identify the addressed ion. Furthermore, the measured pulse duration scales with the rotation angle θ of the implemented gate, which expected to be correlated but slightly longer than the nominal gate time due to deliberate padding introduced to ensure stabilisation of the control hardware.

For the two-qutrit MS gate, we construct a similar circuit, as shown in Fig. 6(b), to observe the corresponding pulse patterns. We expect to see pulses representing two ions being addressed concurrently. As seen in Fig. 8, we indeed observe a clear pattern of which ions are being addressed.

V. MITIGATION STRATEGIES

In general, one of the most fundamental mitigation strategies against any type of attack is to restrict physical access to the QPU. Without such restrictions, attackers could attack the classical control hardware and directly obtain information about quantum circuits and measurement outcomes, thereby bypassing the need for side channels altogether. In general, once side channels are identified, appropriate mitigation strategies are usually clear [44–47]. With respect to the attack described in this work, operators may adopt several targeted countermeasures to protect their QPU. The most intuitive, though arguably unattractive option is to deliberately inject broadband or narrow-band pulsed noise into the frequency range of the RF emanations in order to pollute the leaked signal. However, because quantum information processing is highly susceptible to noise, introducing additional electromagnetic interference, even in frequency bands where one does not expect to drive any interactions, may affect the QPU’s performance.

Table I. Addressing pulse statistics over 200 pulses for single-qubit X gates and MS gates. For each ion, MS gate statistics are computed over all MS gates in which that ion participates.

Ion	X Duration		X Frequency		MS Duration		MS Frequency	
	$\langle\tau\rangle$ (μs)	σ_τ (μs)	$\langle f\rangle$ (MHz)	σ_f (MHz)	$\langle\tau\rangle$ (μs)	σ_τ (μs)	$\langle f\rangle$ (MHz)	σ_f (MHz)
1	40.3	3.1	6.7745	0.0006	232.5	3.8	6.7743	0.0002
2	35.5	3.8	8.112	0.045	229.9	4.1	8.112	0.047
3	34.9	6.8	9.57	0.16	222.3	4.0	9.58	0.16

A more natural countermeasure would consist of improving the electromagnetic shielding of the QPU to suppress RF leakage. However, the feasibility of this approach strongly depends on the experimental environment. On one hand, complete shielding of individual AOMs is impossible due to the required laser apertures or fiber feed-throughs. However, enclosing an entire laboratory-scale setup in a perfect Faraday cage is impractical. In practice, operators must therefore assess the RF leakage of their specific setup and carry out shielding measures tailored to the observed threat level.

Finally, operators may implement control-layer mitigation strategies for the QPU through classical pre-processing and post-processing techniques. A possible countermeasure involves selecting a random subset of the ion register to act as *decoy ions* before executing a circuit. Then, operators may insert random but operationally plausible gates acting on arbitrary transitions of the decoys, yet only keep the measurement results for the computational ions. This way, any circuit reconstructed by attackers is obfuscated by redundant gates, while the intended computation remains unimpeded. Consequently, the use of decoy ions could constitute an efficient countermeasure, whose effectiveness is expected to increase with continued advances in ion-trap technology that enable the confinement and control of larger ion registers.

An alternative avenue, currently pursued for different reasons, is randomized compiling in combination [48–50] with virtual phase-gates. Here, random local unitaries are inserted before and after every computational gate operation. Additionally compilers maximize the use of Z gates over other local operations, since they can be implemented as phase shifts of the driving fields for subsequent gates. As a result, much of the circuit is encoded in phase information which requires more sophisticated instruments to obtain and is randomized shot by shot. Such an approach comes with low overhead and greatly obscures the signal. It would be an interesting question for future research to assess its remaining vulnerability.

VI. CONCLUSIONS

In this work, we identify and exploit a previously unexplored radio-frequency side channel in trapped-ion quantum processors, originating from electromagnetic leakage of the laser modulation infrastructure. After showing that these RF emanations, in principle, carry away all information required to fully reconstruct the quantum circuit carried out on the QPU, we discuss practical considerations and possible attack strategies. Using a non-invasive, low-cost, low-complexity acquisition setup, we experimentally demonstrate that key features of executed quantum circuits, namely ion addressing and gate timing, can be inferred from leaked RF emissions.

While our present implementation is limited in its ability to extract sufficient information for qudit circuit reconstruction, our results establish a clear proof of principle and highlight a realistic security risk for current as well as near-term trapped-ion platforms. In future work, we aim to overcome said limitations by deploying improved antenna designs to discriminate between transitions, thereby gaining access to the qudit manifold used for computations, and by enhancing the signal processing to obtain phase information.

Finally, we point out that both hardware-level shielding and control-level countermeasures can significantly mitigate the threat posed by the described RF side channel. Beyond revealing an imminent risk for potentially proprietary quantum algorithms executed on multi-tenant trapped-ion QPUs, this work underscores the need for systematic assessment of side-channel vulnerabilities in quantum computing architectures as they mature toward broader deployment.

ACKNOWLEDGEMENTS

The authors acknowledge fruitful discussions with Brennan Bell, Phila Rembold, Philipp Schindler, and Andreas Trügler, as well as the experimental support from Keshav Pareek, Manuel John, and Peter Tirlir.

G.G., D.S. and P.E. thank Josef Griesmayr for helpful insights on antennae and Daft Punk for the [soundtrack](#) of this work. This work was funded by the Austrian Federal Ministry of Education, Science, and Research via the Austrian Research Promotion Agency (Forschungsförderungsgesellschaft – FFG) through Quantum Austria project No. 914033. This research was co-funded by the European Research Council (ERC, QUDITS, No. 101039522) and by the European Union (Quantum Flagship project ASPECTS, Grant Agreement No. 101080167). Views and opinions expressed are however those of the authors only and do not necessarily reflect those of the European Union or the European Research Council Executive Agency. Neither the European Union nor the granting authority can be held responsible for them.

* giorgio.grigolo@tuwien.ac.at

† dorian.schiffer@tuwien.ac.at

‡ lukas.gerster@uibk.ac.at

§ martin.ringbauer@uibk.ac.at

¶ paul.erker@tuwien.ac.at

- [1] H.-J. Briegel, T. Calarco, D. Jaksch, J. I. Cirac, and P. Zoller, *Journal of Modern Optics* **47**, 415 (2000).
- [2] C. Nayak, S. H. Simon, A. Stern, M. Freedman, and S. Das Sarma, *Rev. Mod. Phys.* **80**, 1083 (2008).
- [3] H. Häffner, C. Roos, and R. Blatt, *Physics Reports* **469**, 155 (2008).
- [4] M. Saffman, *Journal of Physics B: Atomic, Molecular and Optical Physics* **49**, 202001 (2016).
- [5] S. Slussarenko and G. J. Pryde, *Applied Physics Reviews* **6**, 041303 (2019).
- [6] H.-L. Huang, D. Wu, D. Fan, and X. Zhu, *Science China Information Sciences* **63** (2020), 10.1007/s11432-020-2881-9.
- [7] G. Q. AI and Collaborators, *Nature* **638**, 920 (2025).
- [8] S. C. Wein, T. Goubault de Brugière, L. Music, P. Senellart, B. Bourdoncle, and S. Mansfield, *PRX Quantum* **6**, 040362 (2025).
- [9] M. Liu, R. Shaydulin, P. Niroula, M. DeCross, S.-H. Hung, W. Y. Kon, E. Cervero-Martín, K. Chakraborty, O. Amer, S. Aaronson, A. Acharya, Y. Alexeev, K. J. Berg, S. Chakrabarti, F. J. Curchod, J. M. Dreiling, N. Erickson, C. Foltz, M. Foss-Feig, D. Hayes, T. S. Humble, N. Kumar, J. Larson, D. Lykov, M. Mills, S. A. Moses, B. Neyenhuis, S. Eloul, P. Siegfried, J. Walker, C. Lim, and M. Pistoia, *Nature* **640**, 343 (2025).
- [10] J. Eisert and J. Preskill, “Mind the gaps: The fraught road to quantum advantage,” (2025), [arXiv:2510.19928 \[quant-ph\]](https://arxiv.org/abs/2510.19928).
- [11] D. D. Awschalom, H. Bernien, R. Hanson, W. D. Oliver, and J. Vučković, *Science* **390**, 1004 (2025), <https://www.science.org/doi/pdf/10.1126/science.adz8659>.
- [12] D. Bluvstein, A. A. Geim, S. H. Li, S. J. Evered, J. P. Bonilla Ataides, G. Baranes, A. Gu, T. Manovitz, M. Xu, M. Kalinowski, S. Majidy, C. Kokail, N. Maskara, E. C. Trapp, L. M. Stewart, S. Hollerith, H. Zhou, M. J. Gullans, S. F. Yelin, M. Greiner, V. Vuletić, M. Cain, and M. D. Lukin, *Nature* **649**, 39 (2026).
- [13] A. Morvan, V. V. Ramasesh, M. S. Blok, J. M. Kreikebaum, K. O’Brien, L. Chen, B. K. Mitchell, R. K. Naik, D. I. Santiago, and I. Siddiqi, *Phys. Rev. Lett.* **126**, 210504 (2021).
- [14] Y. Chi, J. Huang, Z. Zhang, J. Mao, Z. Zhou, X. Chen, C. Zhai, J. Bao, T. Dai, H. Yuan, M. Zhang, D. Dai, B. Tang, Y. Yang, Z. Li, Y. Ding, L. K. Oxenløwe, M. G. Thompson, J. L. O’Brien, Y. Li, Q. Gong, and J. Wang, *Nature Communications* **13**, 1166 (2022).
- [15] K. Mato, M. Ringbauer, S. Hillmich, and R. Wille, in *Proceedings of the 28th Asia and South Pacific Design Automation Conference*, ASPDAC ’23 (Association for Computing Machinery, New York, NY, USA, 2023) p. 202–208.
- [16] X. Gao, P. Appel, N. Friis, M. Ringbauer, and M. Huber, *Quantum* **7**, 1141 (2023).
- [17] I. Fernández de Fuentes, T. Botzem, M. A. I. Johnson, A. Vaartjes, S. Asaad, V. Mourik, F. E. Hudson, K. M. Itoh, B. C. Johnson, A. M. Jakob, J. C. McCallum, D. N. Jamieson, A. S. Dzurak, and A. Morello, *Nature Communications* **15**, 1380 (2024).
- [18] M. Meth, J. Zhang, J. F. Haase, C. Edmunds, L. Postler, A. J. Jena, A. Steiner, L. Dellantonio, R. Blatt, P. Zoller, T. Monz, P. Schindler, C. Muschik, and M. Ringbauer, *Nature Physics* **21**, 570 (2025).
- [19] W. K. Wootters and W. H. Zurek, *Nature* **299**, 802 (1982).
- [20] P. C. Kocher, in *Advances in Cryptology — CRYPTO ’96*, edited by N. Kobitz (Springer, Berlin, Heidelberg, 1996) pp. 104–113.
- [21] P. Kocher, J. Jaffe, and B. Jun, in *Advances in Cryptology — CRYPTO ’99*, edited by M. Wiener (Springer, Berlin, Heidelberg, 1999) pp. 388–397.
- [22] K. Gandolfi, C. Mourtel, and F. Olivier, in *Cryptographic Hardware and Embedded Systems — CHES 2001*, edited by Ç. K. Koç, D. Naccache, and C. Paar (Springer, Berlin, Heidelberg, 2001) pp. 251–261.
- [23] D. Genkin, A. Shamir, and E. Tromer, in *Advances in Cryptology — CRYPTO 2014*, edited by J. A. Garay and R. Gennaro (Springer, Berlin, Heidelberg, 2014) pp. 444–461.
- [24] B. Bell and A. Trügler, in *2022 IEEE International Conference on Quantum Computing and Engineering (QCE)* (2022) pp. 259–264.
- [25] B. Bell, A. Trügler, K. Beyer, and P. Erker, “Hardware-agnostic modeling of quantum side-channel leakage via conditional dynamics and learning from full correlation data,” (2026), [arXiv:2602.15966 \[quant-ph\]](https://arxiv.org/abs/2602.15966).
- [26] N. Choudhury, C. N. Mude, S. Das, P. C. Tikkireddi, S. Tannu, and K. Basu, “Crosstalk-induced side channel threats in multi-tenant nisq computers,” (2024), [arXiv:2412.10507 \[cs.ET\]](https://arxiv.org/abs/2412.10507).
- [27] T. Trochatos, C. Kang, F. T. Chong, and J. Szefer, in *2025 26th International Symposium on Quality Electronic Design (ISQED)* (2025) pp. 1–6.
- [28] C. Xu, F. Erata, and J. Szefer, “Exploration of quantum computer power side-channels,” (2023), [arXiv:2304.03315 \[cs.CR\]](https://arxiv.org/abs/2304.03315).
- [29] F. Erata, C. Xu, R. Piskac, and J. Szefer, *IACR Transactions on Cryptographic Hardware and Embedded Systems* **2024**, 735–768 (2024).
- [30] F. Koeune and F.-X. Standaert, “A tutorial on physical security and side-channel attacks,” in *Foundations of Se-*

- curity Analysis and Design III: FOSAD 2004/2005 Tutorial Lectures*, edited by A. Aldini, R. Gorrieri, and F. Martinelli (Springer Berlin Heidelberg, Berlin, Heidelberg, 2005) pp. 78–108.
- [31] A. P. Sayakkara and N.-A. Le-Khac, *IEEE Access* **9**, 113585 (2021).
- [32] Y. M. Ibrahim, S. K. Kermanshahi, K. Kasmarik, and J. Hu, *IEEE Open Journal of the Computer Society* **5**, 511 (2024).
- [33] P. Schindler, D. Nigg, T. Monz, J. T. Barreiro, E. Martinez, S. X. Wang, S. Quint, M. F. Brandl, V. Nebendahl, C. F. Roos, M. Chwalla, M. Hennrich, and R. Blatt, *New Journal of Physics* **15**, 123012 (2013).
- [34] M. Ringbauer, M. Meth, L. Postler, R. Stricker, R. Blatt, P. Schindler, and T. Monz, *Nature Physics* **18**, 1053 (2022).
- [35] L. Gerster, “Towards Scalability of Quantum Processors,” (2024), PhD Thesis.
- [36] A. Sørensen and K. Mølmer, *Phys. Rev. A* **62**, 022311 (2000).
- [37] G. Brennen, S. Bullock, and D. O’Leary, *Quantum Information & Computation* (2006).
- [38] M. Möttönen and J. Vartiainen, *Frontiers in Artificial Intelligence and Applications* (2005).
- [39] Note, even in situations where an attacker may not be able to submit their own circuit, we conclude that they can still distinguish multi-qudit from single-qudit gates, or will resort to a physics-driven strategy.
- [40] G. Acampora, A. Ambainis, N. Ares, L. Banchi, P. Bhardwaj, D. Binosi, G. A. D. Briggs, T. Calarco, V. Dunjko, J. Eisert, O. Ezratty, P. Erker, F. Fedele, E. Gil-Fuster, M. Gärttner, M. Granath, M. Heyl, I. Kerenidis, M. Klusch, A. F. Kockum, R. Kueng, M. Krenn, J. Lässlig, A. Macaluso, S. Maniscalco, F. Marquardt, K. Michielsen, G. Muñoz-Gil, D. Müssig, H. P. Nautrup, S. A. Neubauer, E. van Nieuwenburg, R. Orus, J. Schmiedmayer, M. Schmitt, P. Slusallek, F. Vicentini, C. Weitenberg, and F. K. Wilhelm, “Quantum computing and artificial intelligence: status and perspectives,” (2025), arXiv:2505.23860 [quant-ph].
- [41] L. He, X. Ren, Q. Gao, X. Zhao, B. Yao, and Y. Chao, *70*, 25.
- [42] C. F. Roos, *New Journal of Physics* **10**, 013002 (2008).
- [43] C. Ballance, “High-fidelity quantum logic in Ca+,” PhD Thesis.
- [44] X. Lou, T. Zhang, J. Jiang, and Y. Zhang, *ACM Comput. Surv.* **54** (2021), 10.1145/3456629.
- [45] S. Akter, K. Khalil, and M. Bayoumi, *IEEE Access* **11**, 77543 (2023).
- [46] F. Piessens and P. C. van Oorschot, *IEEE Security & Privacy* **22**, 75 (2024).
- [47] S. R. Bommana, S. Veeramachaneni, S. Ershad, and M. Srinivas, *Scientific Reports* **15**, 13745 (2025).
- [48] J. J. Wallman and J. Emerson, *Phys. Rev. A* **94**, 052325 (2016).
- [49] A. Hashim, R. K. Naik, A. Morvan, J.-L. Ville, B. Mitchell, J. M. Kreikebaum, M. Davis, E. Smith, C. Iancu, K. P. O’Brien, I. Hincks, J. J. Wallman, J. Emerson, and I. Siddiqi, *Phys. Rev. X* **11**, 041039 (2021).
- [50] A. Jain, P. Iyer, S. D. Bartlett, and J. Emerson, *Phys. Rev. Res.* **5**, 033049 (2023).

APPENDIX A: FULL SPECTROGRAMS

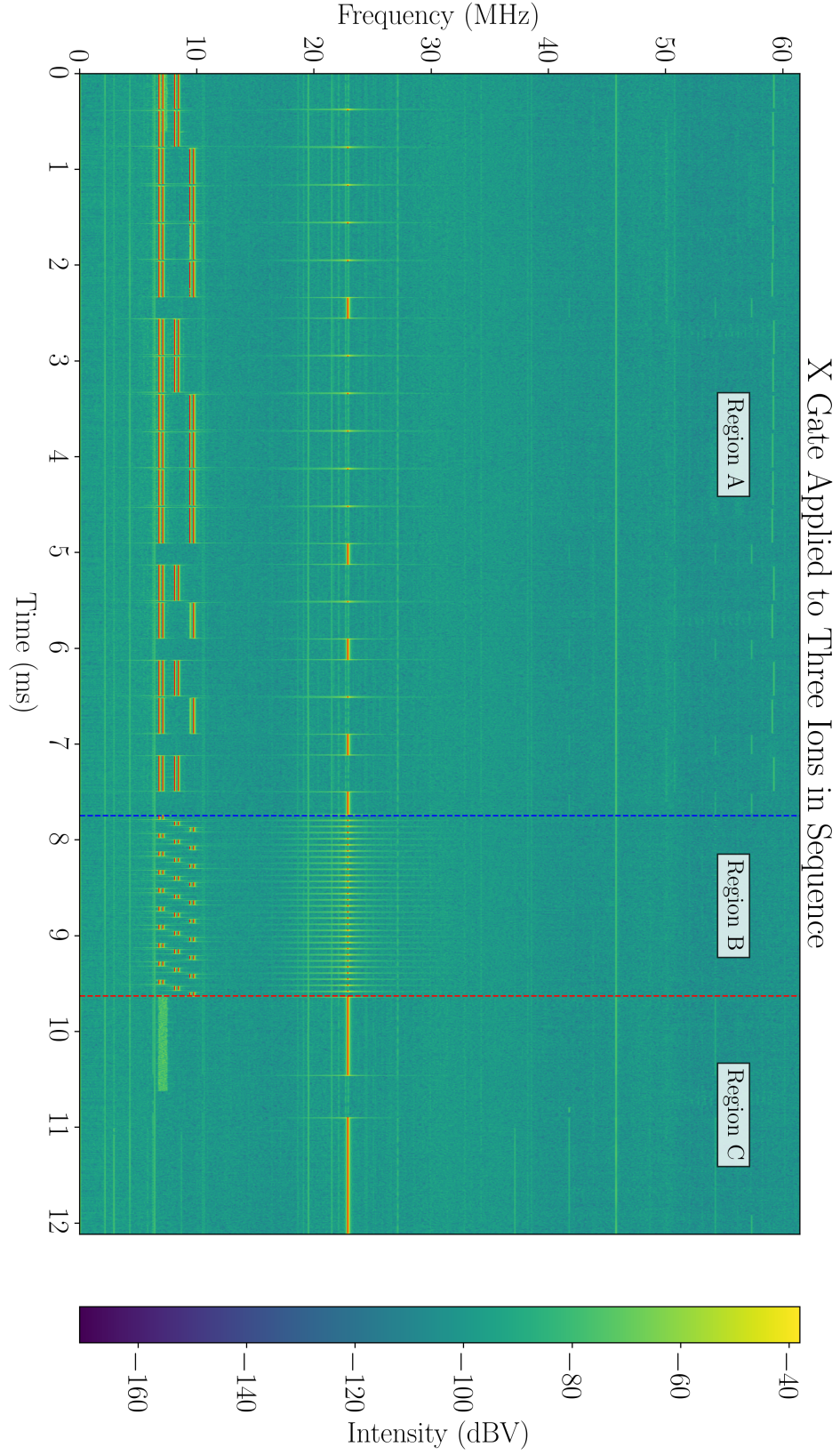


Figure 7. Spectrogram showing sequential $X = R_x^{0,1}(\pi)$ gate applications to three ions. After cooling and initial state preparation (Region A), the gates are applied (Region B), while AODs handle ion addressing. The gate sequence is followed by optical readout pulses (Region C). Pulses that cross our detection threshold are marked in red.

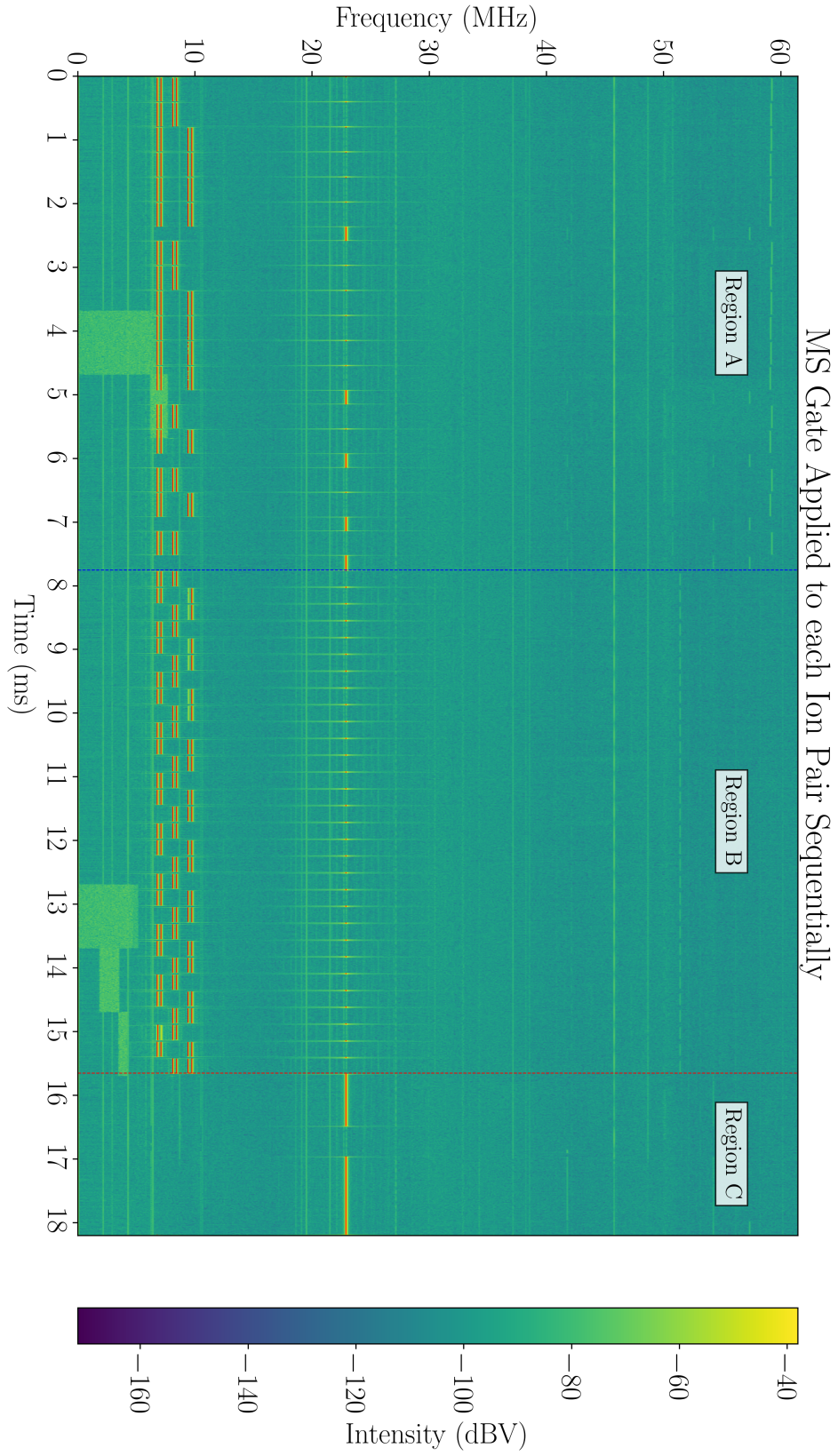


Figure 8. Spectrogram showing sequential $MS = MS^{0,1}$ gate applications to every possible pair of three ions. Here, Regions A and C contain the same pulses as in the corresponding regions in Fig. 7. In Region B, we clearly see the AODs addressing two ions at once, signalling the entangling gate. Again, we mark pulses that lie above our detection threshold in red.